Hindawi
Advances in Civil Engineering
Volume 2018, Article ID 9324956, 18 pages
https://doi.org/10.1155/2018/9324956

Research Article

Theoretical Analysis of Rockfall Impacts on the Soil Cushion Layer of Protective Structures

Xing Wang, Yongxu Xia, and Tianyue Zhou

School of Highway, Chang'an University, Xi'an 710064, Shaanxi, China

Correspondence should be addressed to Xing Wang; 2016021017@chd.edu.cn

Received 10 August 2018; Revised 28 November 2018; Accepted 9 December 2018; Published 26 December 2018

Academic Editor: Luigi Di Sarno

During the Wenchuan Earthquake, with a magnitude of 5.12, collapses and rockfall hazards persisted for a long time after the initial investigations carried out by research fellow S. M. He and his team at the scene of the disaster in October 2008. It is possible that additional incidents of rockfalls in large quantities may continue in the same areas over the next ten to fifteen years. Furthermore, in the vast mountainous region of western China, the topographic relief is evident, and earthquakes occur frequently. Therefore, it is difficult to effectively defend against rockfall hazards. When designing protective structures, the key issue is the analysis of the mechanical response mechanism of the soil cushion layer of the upper cushion when subjected to the impact of rockfall. As such, a theoretical method was used to perform such an analysis. The cavity expansion and energy conservation model were adopted. Analytical solutions for the impact force and penetration depth were then derived. Furthermore, the impact force and penetration depth of rockfall were studied with the LS-DYNA software to obtain values for the impact forces and the penetration depth. Finally, the reliability of the theoretical method was evaluated using the cavity expansion, energy conservation, numerical simulation, Hertz, Japanese, Swiss, Australian, B. S. Guan, tunnel manual, and subgrade methods based on an engineering model. The results show that the cavity expansion and the energy conservation methods yielded consistent results. Meanwhile, the cavity expansion and the energy conservation methods also yielded consistent results with the numerical simulation, Japanese (obtained by laboratory experiment), Swiss (obtained by laboratory experiment), and Australian (obtained by field experiment) methods. The relevant methods and conclusions shall therefore be applied to the design of rockfall protection structure in future investigations.

1. Introduction

As a key aspect in the engineering of highway routes, the technology for building tunnels has gradually improved over time [1–3]. Shed tunnel protection structures are special tunnel structures. These structures and others such as open cut tunnels and passive protective structures in hazardous areas are designed primarily to protect against the impact forces of rockfall. In order to avoid immediate impact load on protected structures, a soil layer of a certain thickness is generally used [4]. During the rockfall impact on the soil cushion layer, the time interval is short and the energy conversion is complicated. In addition, elastoplastic deformation of the soil cushion layer occurs. Therefore, the impact process of the rockfall is a complex impact dynamics problem. In the design of protective structures, the key issue is the analysis of the mechanical response mechanism of the soil cushion layer under the impact of rockfall.

Many scholars and research institutes are directing increasing attention to rockfall disaster research. The classic Hertz contact theory and Thornton elastoplastic impact theory have been applied widely [5–8]. Johnson described in his book "Contact Mechanics" the details of the mechanical properties of an object under the effects of static contact, sliding, rolling, and impact [9]. Labiouse et al. presented a semiempirical and semitheoretical method to analyze rockfall impact forces based on impact experiments (hereinafter referred to as the Swiss method) [10]. Kishi and Ikeda studied the mechanical response characteristics of a retaining wall under rockfall impact based on field experiments and numerical simulations [11]. Heidenreich and Labiouse studied the mechanical characteristics of a slope

with a loose structure under the impact of rockfall using small-scale model experiments [12]. Calvetti and Prisco analyzed the mechanical response characteristics of gravel soil under rockfall impact based on experiments and numerical simulations [13]. Based on the field test method and the theorem of impulse, Pichler and Hillmich developed a calculation method for impact force and penetration depth associated with rockfall (hereinafter referred to as the Australian method) [7]. Mougin et al. examined the mechanical response of rockfall on a concrete plate under direct impact conditions based on model experiments [14]. Delhomme et al. adopted model experiments and numerical simulations to analyze the energy dissipation and seismic mitigation effects of the new type of shed tunnel structures [15]. The Japanese Road Association developed a semi-empirical and semitheoretical calculation method for rockfall impact force using model experiments (hereinafter referred to as the Japanese method) [16]. Calvetti and Prisco analyzed the design method for shed tunnel structures based on the uncoupled calculation method [17]. Ye and Chen performed a comparative study on rockfall impact force values by employing the Japanese, Swiss, and Hertz methods in conjunction with an engineering model [18].

Ye et al. analyzed the rockfall impact forces under oblique impact on the soil cushion layer [19]. Qi et al. set up an analysis model for rockfall impact forces based on a theoretical approach and studied the amplification coefficient of rockfall impact forces [20]. Yuan et al. analyzed the influence of the weight, shape, falling height, and impact angle of rockfall on the impact force based on experiments [21]. Sun et al. attempted to add discarded tires to the soil cushion layer and investigated the impact resistance of the new cushion structure via an experimental approach [22]. Zhang et al. investigated the mechanical response mechanism of oil/gas pipe under rockfall impact using a numerical simulation method [23]. Hu et al. discovered the law of jumping range of rockfall based on three influential factors: shape, weight, and the release altitude of rockfall using an experimental method [24]. Lam et al. studied the overturning stability of L-shaped rigid barriers subjected to rockfall impacts [25]. Basharat et al. analyzed the effects of volume and topographic parameters on rockfall travel distance based on a case study from the NW Himalayas, Pakistan [26].

Zhu et al. analyzed particle size and the thickness of the gravel cushion layer on the restitution coefficient of rockfall in rockfall impact procession [27]. Luo et al. experimentally studied the rockfall impact force of the frame shed tunnel structure [28]. Asteriou and Tsiambaos analyzed the effect of rockfall impact velocity, block mass, and hardness on rockfall restitution coefficients [29]. Toe et al. adopted a metamodel hazard mitigation strategy to improve the effectiveness of rockfall protection barriers [30]. Wang et al. adopted an experimental approach to analyzing the mechanical response law of an EPS cushion layer under rockfall impact [31]. Bhatti combined experimental and numerical simulation methods to study the energy dissipation property of the EPS cushion layer under the impact of rockfall [32]. Bi et al. adopted a numerical simulation method to analyze the mechanical response mechanism of a bumper plate under the rockfall impact [33]. Yu et al. studied the maximum impact force of rockfall using an experimental approach [34]. Zhang et al. devised an estimation model for calculating the maximum impact force of rockfall based on contact theory and verified this model experimentally [35]. Yan et al. utilized numerical simulations to analyze the mechanical response mechanism of reinforced concrete slabs under the impact of rockfall [36].

Prof. B. S. Guan proposed a calculation method for impact forces and penetration depth based on experiments. Further, he considered the effect on the thickness of the soil cushion layer (hereinafter referred to as the B. S. Guan method) [37]. Using the theory of momentum, the impact force and penetration depth are given in the *Technical Manual for Railway Engineering Design Tunnel* (*Revised Edition*) (hereinafter referred to as the tunnel manual method). In addition, in *Code for Design of Highway Subgrade* of China, the rockfall impact force and penetration depth are given based on the work-energy principle (hereinafter referred to as the subgrade method).

The Japanese, Swiss (based on indoor experiments), and Australian methods (based on field tests) are three classical methods for the design of protection structures. However, these three methods are all semitheoretical and semiempirical. Moreover, few scholars have focused on theoretical derivations to obtain the penetration depth and impact force. Meanwhile, some researchers have indicated that the value of the impact force is small in China [18].

Based on the dynamic cavity expansion model and the energy conservation model, a theoretical mechanical system of rockfall impacting the soil cushion layer is established and analytic solutions of rockfall impact force and penetration depth are obtained. In addition, the LS-DYNA software is used to analyze the change laws of impact force and penetration depth during rockfall impact processes. Finally, this study will compare and analyze the calculation results for penetration depth and impact forces calculated based on the cavity expansion, energy conservation, numerical simulation, Japanese, Swiss, Australian, Hertz, B. S. Guan, tunnel manual, and subgrade methods.

2. Conventional Classical Calculation Theories

2.1. Hertz Method. In 1985, Hertz derived expressions for the maximum deformation and maximum impact based on elastic theory.

$$\text{Impact force:}\quad F = \frac{32\sqrt{3}}{27} E\sqrt{R}\left[\frac{45\sqrt{3}\,M v_0^2}{128R^{1/2}E}\right]^{3/5},$$
$$\text{Penetration depth:}\quad L = \left[\frac{45\sqrt{3}\,M v_0^2}{128R^{1/2}E}\right]^{2/5}, \tag{1}$$

where F is the rockfall impact force, E is the elasticity modulus of soil cushion layer, R is the radius of the rockfall, M is the mass of the rockfall, v_0 is the initial velocity of

rockfall, and L is the penetration depth of the rockfall impact.

2.2. Swiss Method. In 1996, a Swiss scholar, Labiouse, developed the relevant empirical method for rockfall impact forces based on rockfall experiments.

$$\text{Impact force: } F = 1.765 \cdot M_{\mathrm{E}}^{2/5} \cdot R^{1/5} \cdot (QH)^{3/5}, \tag{2}$$

where M_{E} is the deformation modulus of soil cushion layer, Q is the quality of rockfall, and H is the falling height of the rockfall.

2.3. Japanese Method. In 2000, based on rockfall experiments and combined with Hertz elastic theory, the Japanese Road Association presented the relevant semiempirical and semitheoretical calculation method of rockfall impact forces.

$$\begin{aligned} &\text{Impact force: } F = 2.108 \cdot (Mg)^{2/3} \cdot \lambda^{2/5} \cdot H^{3/5}, \\ &\text{lame constant: } \lambda = \frac{\upsilon E}{(1+\upsilon(1-2\upsilon))}, \end{aligned} \tag{3}$$

where g is the gravitational acceleration, λ is the lame constants, and υ is the Poisson's ratio of soil cushion layer.

2.4. Australian Method. In 2005, Australian scholar Pichler proposed the semiempirical and semitheoretical calculation method of rockfall impact force and penetration depth combined with the rockfall field test.

$$\begin{aligned} &\text{Impact force: } F = \frac{2Mv_0}{t_{\mathrm{w}}} = \frac{Mv_0^2}{L}, \\ &\text{Impact time: } t_{\mathrm{w}} = \frac{2L}{v_0}, \\ &\text{Penetration depth: } \begin{cases} L = D\sqrt{\dfrac{103500H}{R_{\mathrm{c}} + 19180H}}, & \left(\dfrac{L}{D} \le 1.257\right), \\ L = D\left\{1.518 \ln\left[\dfrac{1 + 19182.39\left(H/R_{\mathrm{c}}\right)}{1.414}\right] + 1.257\right\}, & \left(\dfrac{L}{D} \ge 1.257\right), \end{cases} \end{aligned} \tag{4}$$

where t_{w} is the impact time of the rockfall, D is the diameter of the rockfall, and R_{c} is the indentation resistance of target materials.

2.5. B. S. Guan Method. In 1996, the scholar B. S. Guan established the empirical method of impact force and penetration depth based on laboratory experiments. This method considers the influence of the thickness of the soil cushion layer on impact force.

$$\begin{aligned} &\text{Impact force: } F_{\max} = \zeta Ma, \\ &\text{Acceleration: } a = \frac{\sqrt{2gH}}{t_{\mathrm{w}}}, \\ &\text{Impact time: } t_{\mathrm{w}} = \frac{1}{100}\left[0.097Mg + 2.21h + \frac{0.045}{H} + 1.2\right], \\ &\text{Penetration depth: } L = \kappa\sqrt{\frac{QH}{10}}, \end{aligned} \tag{5}$$

where ζ is the correction coefficient of the rockfall impact force, κ is the coefficient of rockfall penetration depth, a is the acceleration of the rockfall impact, and h is the thickness of soil cushion layer.

2.6. Method of Tunnel Manual. The method of tunnel manual refers to an approach recommended in *Technical Manual for Railway Engineering Design Tunnel (Revised Edition)*, and in essence, it is also an approximation method of the theorem of momentum.

$$\begin{aligned} &\text{Impact force: } F = \frac{Qv_0}{gt_{\mathrm{w}}}, \\ &\text{Impact time: } t_{\mathrm{w}} = \frac{2h}{c}, \\ &\text{Compression wave velocity: } c = \sqrt{\frac{1-\upsilon}{(1+\upsilon)(1-2\upsilon)} \cdot \frac{E}{\rho_0}}, \\ &\text{Penetration depth: } L = v_0\sqrt{\frac{Q}{2g\gamma\psi}} \\ &\qquad \times \sqrt{\frac{1}{2\mathrm{tg}^4\left(45^\circ + \varphi^*/2\right) - 1}}, \end{aligned} \tag{6}$$

where c is the reciprocating velocity of compression waves in the soil cushion layer, γ is the specific gravity of the soil cushion layer, ψ is the cross-sectional area of an equivalent sphere for rockfall, φ^* is the inner friction angle of soil

cushion layer, and ρ_0 is the density before deformation of spherical cavity microbody.

2.7. Subgrade Method. *Code for Design of Highway Subgrade* provides a computational formula for rockfall impact force and penetration depth based on the work-energy principle.

$$\text{Impact force: } F = 2\gamma L\left[2\text{tg}^4\left(45^\circ + \varphi^*/2\right) - 1\right]\psi,$$

$$\text{Penetration depth: } L = v_0\sqrt{\frac{Q}{2g\gamma\psi}} \times \sqrt{\frac{1}{2\text{tg}^4\left(45^\circ + \varphi^*/2\right) - 1}}. \tag{7}$$

3. Theoretical Analysis Based on Dynamic Cavity Expansion Model

The spherical expansion model is widely applied to penetration mechanical model analysis. In this section, the impact of rockfall on a soil cushion layer is simplified by considering the normal impact of a rigid ball on a semi-infinite soil cushion layer.

By referring to Figure 1, the normal stress of point A on the soil cushion layer σ_A could be calculated using $\sigma_{\text{rq}(A)}$ of the cavity expansion sphere at the same position A, so a series of spherical cavities originating from the bottom of the sphere could be used to simulate the process of crater formation due to rockfall impact on the soil cushion layer. The radius of these cavity spheres gradually increases from 0 to r_q, thus forming the so-called dynamic spherical cavity expansion model.

The radius of cavity expansion sphere $r_\text{q}(A)$ is

$$r_\text{q}(A) = \frac{x_A}{\sin\alpha}, \tag{8}$$

where $r_\text{q}(A)$ is the radius of the spherical cavity, x_A is the x coordinate value of point A, and α is the acute angle between the normal line and the vertical line at point A.

During the normal impact of rockfall on the soil cushion layer at a velocity of v_h, the velocity of the dynamic spherical cavity expansion is

$$v_\text{q} = \dot{r}_\text{q} = v_\text{h}\cos\alpha, \tag{9}$$

where v_q is the velocity of spherical cavity expansion, $\dot{r}_\text{q}$ is the expansion velocity of spherical cavity, and v_h is the velocity of rockfall impact.

And the acceleration of the dynamic cavity expansion is

$$\dot{v}_\text{q} = \ddot{r}_\text{q} = \dot{v}_\text{h}\cos\alpha, \tag{10}$$

where $\dot{v}_\text{q}$ is the acceleration of spherical cavity expansion, $\ddot{r}_\text{q}$ is the expansion acceleration of spherical cavity, and $\dot{v}_\text{h}$ is the acceleration of a rockfall impact.

3.1. Mechanical Analysis of Microunit with Spherical Coordinates. As shown in Figure 2, the Euler coordinate of spherical coordinates is employed to perform mechanical analysis on the selected microbody.

By referring to Figure 2, a mechanical analysis of the microbody selected yields equation (7) according to the theorem of momentum:

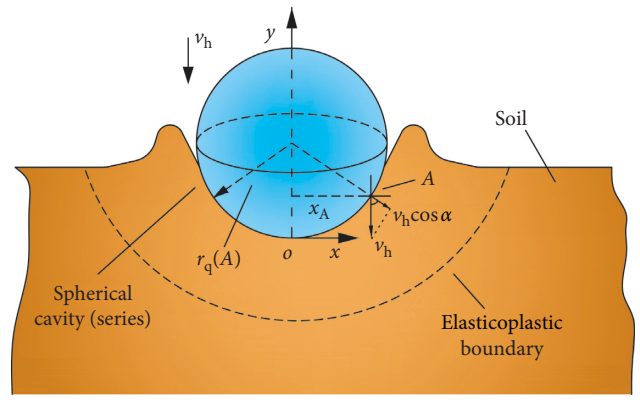

Figure 1: Force and displacement of spherical cavity microelement.

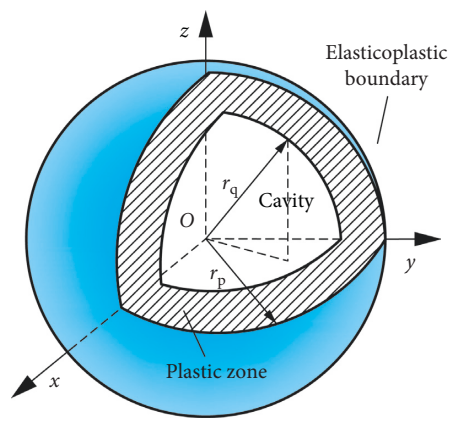

Figure 2: Spherical cavity.

$$\left\{\begin{array}{l}(\sigma_\text{r} + d\sigma_\text{r})\left[(r + dr)\,d\theta\right]^2 - \sigma_\text{r}(r\,d\theta)^2 \\ -4\sigma_\theta\,dr\,(r\,d\theta)\sin\dfrac{d\theta}{2}\end{array}\right\}dt = -\rho_0\,dv(r\,d\theta)^2\,dr, \tag{11}$$

where σ_r is the radial stress of the spherical cavity microbody, σ_θ is the hoop stress of the spherical cavity microbody, r is the distance from the coordinate origin to the mass point of the spherical cavity microbody, v is the moving velocity of the mass point of the spherical cavity microbody, and θ is the opening angle of spherical cavity microbody.

The velocity of the mass point of the microbody in this coordinate is

$$v = \frac{\partial s}{\partial t} + v\frac{\partial s}{\partial r}, \tag{12}$$

where s is the displacement of the mass point of the spherical cavity microbody and t is the moving time of the mass point of the spherical cavity microbody.

And the acceleration of the mass point could be expressed by formula (8):

$$\frac{dv}{dt} = \frac{\partial v}{\partial t} + v\frac{\partial v}{\partial r}. \tag{13}$$

For the smaller $d\theta$, $\sin(d\theta/2)$ could be expressed as approximately $d\theta/2$. Substituting this simplified relation into

formula (11) and dividing both sides of the simplified equation by $r^2 dr\, d\theta^2$, if the high order trace is omitted, considering equations (11) and (13), we obtain

$$\frac{\partial \sigma_r}{\partial r} + \frac{2(\sigma_r - \sigma_\theta)}{r} = -\rho_0\left(\frac{\partial v}{\partial t} + v\frac{\partial v}{\partial r}\right). \tag{14}$$

Figure 3 represents the force and displacement of a spherical cavity microelement.

Combined with the law of conservation of mass, we obtain

$$(r\, d\theta)^2\, dr \cdot \rho_0 = \rho\left[(r-s)\, d\theta\right]^2 d(r-s), \tag{15}$$

where ρ is the density after deformation of spherical cavity microbody.

After the partial derivative of equation (15), we obtain

$$\frac{1}{3}\frac{\partial}{\partial r}\left[(r-s)^3\right] = \frac{\rho_0}{\rho} r^2. \tag{16}$$

Taking the integral of equation (16) and assuming the medium of the plastic zone is incompressible, we obtain

$$(r-s)^3 = r^3 + f(t), \quad \left(r_q \le r\right). \tag{17}$$

Further, combined with the boundary conditions of $r = r_q$, $s = r_q$, we obtain the displacement of the microbody, as follows:

$$s = r\left[1 - \left(1 - \frac{r_q^3}{r^3}\right)^{1/3}\right], \tag{18}$$

where r_q is the radius of spherical cavity.

Combined with equations (18) and (12), we obtain an expression for the velocity of the microbody, as follows:

$$v = \frac{r_q^2}{r^2}\frac{dr_q}{dt}. \tag{19}$$

According to the continuous medium assumption, the expression of for the velocity shall be applied to the medium of both elastic and plastic zones.

3.2. Mechanical Analysis of the Elastic Zone. After rockfall impact on the soil cushion layer, the elastic zone formed within this layer has the following relationships:

(1) Physical equation

$$\begin{cases} \varepsilon_r = \dfrac{\sigma_r - 2\upsilon\sigma_\theta}{E}, \\ \varepsilon_\theta = \dfrac{(1-\upsilon)\sigma_\theta - \upsilon\sigma_r}{E}, \end{cases} \tag{20}$$

(2) Geometric equation

$$\begin{cases} \varepsilon_r = -\dfrac{\partial s}{\partial r}, \\ \varepsilon_\theta = -\dfrac{s}{r}, \end{cases} \tag{21}$$

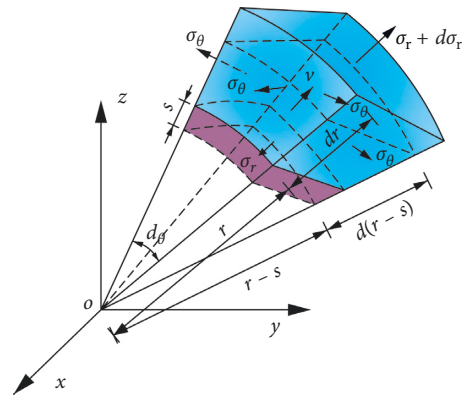

Figure 3: Force and displacement of spherical cavity microelement.

where ε_r is the radial strain of spherical cavity microbody and ε_θ is the hoop strain of spherical cavity microbody.

Substituting the expression for the displacement of the microbody s into equation (21) and using a Taylor series to expand, only the first two terms of the expansion are substituted into equation (20) on the premise of ensuring the effectiveness of the calculation results. We then obtain

$$\sigma_r - \sigma_\theta = \frac{E}{(1+\upsilon)}\left(\frac{r_q}{r}\right)^3. \tag{22}$$

Combining equations (22), (19), and (14), we obtain

$$\frac{\partial \sigma_r}{\partial r} + \frac{2Er_q^3}{(1+\upsilon)r^4} = -\rho_0\left(\frac{2r_q\dot{r}_q + r_q^2\ddot{r}_q}{r^2} - \frac{2r_q^4\dot{r}_q^2}{r^5}\right). \tag{23}$$

Considering the boundary conditions $r \longrightarrow \infty$ and $\sigma_r = 0$ and taking the integral of equation (23), we obtain

$$\sigma_r = \frac{2Er_q^2}{3(1+\upsilon)r^3} + \frac{2\rho_0 r_q\dot{r}_q^2 + \rho_0 r_q^2\ddot{r}_q}{r} - \frac{\rho_0\dot{r}_q^2 r_q^4}{2r^4}. \tag{24}$$

3.3. Mechanical Analysis of Plastic Zone. For the ideal elastic-plastic soil cushion layer in the case of shear failure of the soil cushion layer, combined with Thornton's theory, equation (25) is established:

$$\sigma_r - \sigma_\theta = 2\tau_0. \tag{25}$$

Combined with the dynamic strength theory proposed by Richart, τ_0 can be determined using equation (26):

$$\tau_0 = K\tau, \tag{26}$$

where τ_0 is the shear strength of soil cushion layer, τ is the undrained shear strength of soil cushion layer, and K is the shear strength coefficient of soil cushion layer.

Considering equations (22), (19), and (14), we obtain

$$\frac{\partial \sigma_r}{\partial r} + \frac{4\tau_0}{r} = -\rho_0\left(\frac{2r_q\dot{r}_q + r_q^2\ddot{r}_q}{r^2} - \frac{2r_q^4\dot{r}_q^2}{r^5}\right). \tag{27}$$

Taking the boundary conditions $r = r_q$ and $\sigma_r = \sigma_{rq}$ into account, we obtain

$$\sigma_r = \sigma_{rq} + 4\tau_0 \ln\left(\frac{r_q}{r}\right) - \frac{3\rho_0 \dot{r}_q^2}{2} + \rho_0 r_q \ddot{r}_q - \frac{2\rho_0 r_q \dot{r}_q^2 + \rho_0 r_q^2 \ddot{r}_q}{r} + \frac{\rho_0 r_q^4 \dot{r}_q^2}{2r^4}, \tag{28}$$

where σ_{rq} is the radial stress on the spherical cavity surface.

Using the boundary conditions of $r = r_p$ and $\sigma_{rq}^- = \sigma_{rq}^+$ according to the assumption of the soil cushion layer being in the elastic-plastic zone and substituting the boundary conditions into equation (24) and (28), respectively, we can obtain an expression for the normal stress on the surface of cavity σ_{rq}.

$$\sigma_{rq} = \frac{2E}{3(1+\upsilon)}\left(\frac{r_q}{r_p}\right)^3 - 4\tau_0 \ln\left(\frac{r_q}{r_p}\right) + \frac{3\rho_0 \dot{r}_q^2}{2} + \rho_0 r_q \ddot{r}_q, \tag{29}$$

where r_p is the plastic region radius of spherical cavity.

Combining equations (22) and (25), we obtain

$$\frac{r_q}{r_p} = \sqrt[3]{\frac{2\tau_0(1+\upsilon)}{E}}. \tag{30}$$

Substituting equation (30) into (29), we obtain

$$\sigma_{rq} = \frac{4\tau_0}{3}\ln\left[\frac{eE}{2\tau_0(1+\upsilon)}\right] + \frac{3\rho_0 v_q^2}{2} + r_q \rho_0 \frac{dv_q}{dt}. \tag{31}$$

The process of rockfall impact on cratering can be imitated through a series of infinitesimal cavity expansion originating from the bottom of the sphere. As shown in Figure 4, for the horizontal infinitesimal cavity that lies at point G, the cavity radius gradually increases from 0 to $r_q(G)$, and then forms the final infinitesimal cavity Q_G. The formation process for the infinitesimal cavity Q_N is also the same. Further, we perform an integration to analyze the entire process for the impact of rockfall on Earth mass.

From Figure 4, the velocity and acceleration of the dynamic cavity expansion are

$$\begin{cases} v_q = \dot{r}_q = v_h \cos\varphi, \\ \dot{v}_q = \ddot{r}_q = \dot{v}_h \cos\varphi, \end{cases} \tag{32}$$

where φ is the acute angle between the tangent at the spherical cavity surface through point G with x axis.

The value of $\cos\varphi$ is determined using relevant geometrical relations. A tangent line of the cavity is made through point G to obtain the geometrical relation expression as follows:

$$y = R - \sqrt{R^2 - x^2}, \tag{33}$$

where x is the x coordinate value of point G on spherical cavity and y is the y coordinate value of point G on spherical cavity.

Since L_1 is the tangent line through point G, we obtain

$$y_1' = \tan\varphi, \tag{34}$$

where y_1' is the slope of the tangent line L_1.

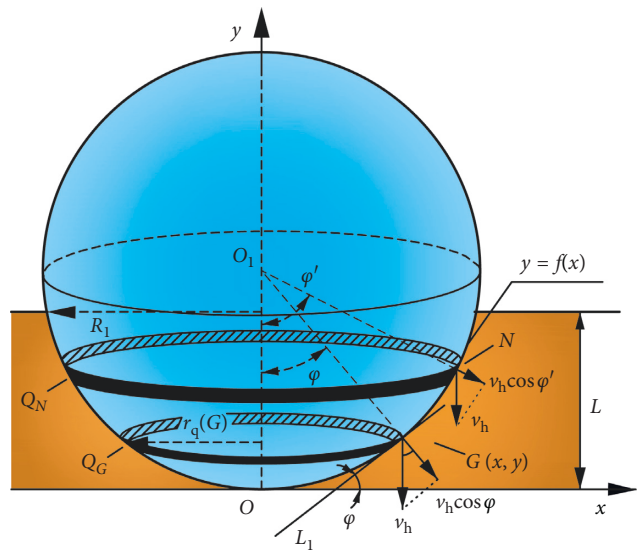

Figure 4: Dynamic cavity of analysis of rockfall.

According to the trigonometric function relation,

$$\begin{cases} \sec^2\varphi - 1 = \tan^2\varphi, \\ \sec\varphi = \cos^{-1}\varphi, \end{cases} \tag{35}$$

and we can combine equations (33)–(35) to obtain

$$\cos\varphi = \frac{1}{\sqrt{1 + (y_1')^2}}. \tag{36}$$

3.4. Impact Force. Equation (31) is the expression of the normal stress on the surface of cavity σ_{rq}, over which the integral is performed so as to obtain the impact force of the rockfall.

$$F = 2\pi \int_0^{R_1} x\sigma_{rq} \frac{dx}{dl} \cdot dl = 2\pi \int_0^{R_1} x\sigma_{rq}\, dx, \tag{37}$$

where R_1 is the radius of the horizontal infinitesimal cavity at the upper surface of soil cushion layer, and l is the width value of infinitesimal cavity.

R_1 is calculated according to the equation below:

$$R_1 = \sqrt{R^2 - (R-L)^2} = \sqrt{2RL - L^2}. \tag{38}$$

Combined equations (31), (32), (37), and (38), and given that when $r_q = R$ and $L_{max} \le R$, the impact force of rockfall on the soil cushion layer shall be calculated according to equation (39):

$$F_1 = \frac{4\pi\tau_0}{3}\left(2RL - L^2\right)\ln\left[\frac{eE}{2\tau_0(1+\upsilon)}\right] + \frac{3\pi\rho_0\left[R^4 - (R-L)^4\right]v_h^2}{4R^2} + \frac{2\pi\rho_0\left[R^3 - (R-L)^3\right]}{3}\frac{dv_h}{dt}, \tag{39}$$

where F_1 is the rockfall impact force.

Generally, the velocity of rockfall for the calculation is 4–24 m/s. For the convenience of calculation, we omit $3\rho_0 v_q^2/2$ and $r_q\rho_0(dv_q/dt)$, in equation (31), so equation (31) can be rewritten as

$$\sigma_{rq} = \frac{4\tau_0}{3}\ln\left[\frac{eE}{2\tau_0(1+v)}\right], \tag{40}$$

and equation (39) for the calculation of the impact force can be simplified into

$$F_2 = \pi\left(2RL - L^2\right)\frac{4\tau_0}{3}\ln\left[\frac{eE}{2\tau_0(1+v)}\right], \tag{41}$$

where F_2 is the rockfall impact force.

During the rockfall impact process of the rolling stone, when $L_{max} \geq R$, the value of R can be substituted into that of L in equation (37) and (41).

3.5. Penetration Depth. Combined with Newton's second law, we obtain the relation between the impact of velocity of rockfall and penetration depth:

$$\frac{dv_h}{dt} = v_h\frac{dv_h}{dL}. \tag{42}$$

During the impact process, if the velocity and acceleration of the rockfall are not considered for the influence on penetration depth, and when $L_{max} \leq R$, we multiply the rockfall mass M on both ends of equation (42) and obtain the equation for the impact force as follows:

$$F_2 = -Mv_h\frac{dv_h}{dL}, \tag{43}$$

where L_{max} is the maximum penetration depth of the rockfall by the cavity method.

That is,

$$\frac{4\pi\tau_0}{3}\left(2RL - L^2\right)\ln\left[\frac{eE}{2\tau_0(1+v)}\right] = -Mv_h\frac{dv_h}{dL}. \tag{44}$$

Combined with the initial conditions of $v_h = v_0$ and $L = 0$ and taking the integral of equation (44), we obtain

$$\frac{4\pi\tau_0}{3M}\left(RL^2 - \frac{L^3}{3}\right)\ln\left(\frac{eE}{2\tau_0(1+v)}\right) = \frac{\left(v_0^2 - v_h^2\right)}{2}. \tag{45}$$

From equation (45), we can obtain the penetration depth of rockfall at any time when the velocity is v_h, during the period in which impact velocity decreases from v_0 to 0. When $v_h = 0$, we obtain the maximum penetration depth of the rockfall L_{max}.

$$\frac{4\pi\tau_0}{3M}\left(RL_{max}^2 - \frac{L_{max}^3}{3}\right)\ln\left[\frac{eE}{2\tau_0(1+v)}\right] = \frac{v_0^2}{2}. \tag{46}$$

If the calculation result satisfies $L_{max} \geq R$, in equation (44), we set $L = R$.

If the influence of rockfall velocity and acceleration during the impact process is considered and when $L_{max} \leq R$, we obtain

$$F_1 = -Mv_h\frac{dv_h}{dL}. \tag{47}$$

Substituting equations (39) into (47), we obtain

$$\frac{dv_h}{dL} = -\frac{(4\tau_0/3)\ln\left[eE/(\tau_0(1+v))\right](2\pi RL - \pi L^2) + \left(\left(3\pi\rho_0\left[R^4 - (R-L)^4\right]\right)/4R^2\right)v_h^2}{\left\{M - \left((2\pi\rho_0)/3\right)\left[R^3 - (R-L)^3\right]\right\}v_h}. \tag{48}$$

Considering the initial conditions of $v_h = v_0$ and $L = 0$, when the calculation result for the penetration depth does not satisfy $L_{max} \geq R$, in equation (45), we set $L = R$. Using an analytical method, we can obtain the relation between L and v_h.

Using equation (48), we obtain

$$F = \frac{M\left\{(4\tau_0/3)\ln\left[eE/(2\tau_0(1+v))\right](2\pi RL - \pi L^2) + \left(\left(3\pi\rho_0\left[R^4 - (R-L)^4\right]\right)/4R^2\right)v_h^2\right\}}{\left\{M - \left((2\pi\rho_0)/3\right)\left[R^3 - (R-L)^3\right]\right\}}. \tag{49}$$

We can substitute the values of L and v_h obtained using the analytical method into equation (49), to calculate the value of the impact force F.

4. Theoretical Derivation Based on Energy Conservation Model

In this section, the impact of rockfall on the soil cushion layer is simplified into the normal impact of a rigid ball on a semi-infinite soil cushion layer, and further derivation is based on the principle of conservation of energy.

During the process of rockfall impact on the soil cushion layer, there are four main forms of energy:

(1) Initial kinetic energy of rockfall at the moment of contact with the cushion layer

(2) Plastic deformation and friction generate forms of energy dissipation

(3) Microgravitational potential energy of rockfall during the impact process

4.1. Surface Stress Analysis of Cylindrical Cavity. After rockfall impact on the cushion layer, we take the cross section of a cylindrical cavity with a radius of r_q, and the plastic zone and elastic zone are shown in Figure 5.

We then consider the microbody as shown in Figure 6 during mechanical analysis. The value of displacement of the microbody is positive in the outward direction, and the values of the stress σ_r^* and σ_θ^* and strain ε_r^* and ε_θ^* are positive with pressure.

So, we obtain the equation below:

$$\frac{\partial \sigma_r^*}{\partial r^*} + \frac{(\sigma_r^* - \sigma_\theta^*)}{r^*} = 0, \tag{50}$$

where σ_r^* is the radial stress of the cylindrical cavity microbody, σ_θ^* is the hoop stress of the cylindrical cavity microbody, and θ^* is the opening angle of cylindrical cavity microbody.

Further, in the elastic zone, the geometric relation is given by equation (51):

$$\begin{cases} \varepsilon_r^* = -\dfrac{\partial s^*}{\partial r^*}, \\ \varepsilon_\theta^* = -\dfrac{s^*}{r^*}, \end{cases} \tag{51}$$

where ε_r^* is the radial strain of cylindrical cavity microbody and ε_θ^* is the hoop strain of cylindrical cavity microbody.

For the medium of the elastic zone, according to Hooke's law and the reference *Cavity Expansion Methods in Geomechanics* [38], the elastic relation expression is given by equation (52):

$$\sigma_r^* - \sigma_\theta^* = \frac{E(\varepsilon_r^* - \varepsilon_\theta^*)}{(1+v)}. \tag{52}$$

Further, according to the law of the conservation of mass, we obtain

$$\frac{1}{2}\frac{\partial}{\partial r^*}\left[(r^* - s^*)^2\right] = \frac{\rho_0^*}{\rho^*} r^*, \tag{53}$$

where r^* is the distance from the coordinate origin to the mass point of the cylindrical cavity microbody, s^* is the displacement of the mass point of the cylindrical cavity microbody, ρ_0^* is the density before deformation of cylindrical cavity microbody, and ρ^* is the density after deformation of cylindrical cavity microbody.

Here, we consider that only the medium of the elastic zone is compressed, so we obtain

$$\frac{\partial}{\partial r^*}\left[(r^* - s^*)^2\right] = 2r^*. \tag{54}$$

Considering the boundary conditions $r^* = r_q^*$, $s^* = r_q^*$ and taking the integral of equation (65), we obtain the expression for the displacement of a microbody:

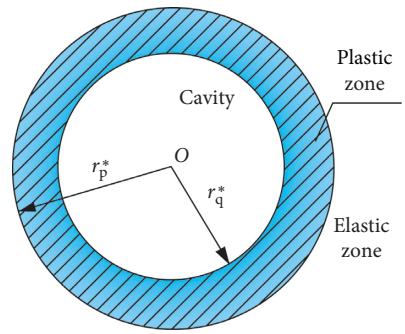

Figure 5: Cylindrical cavity.

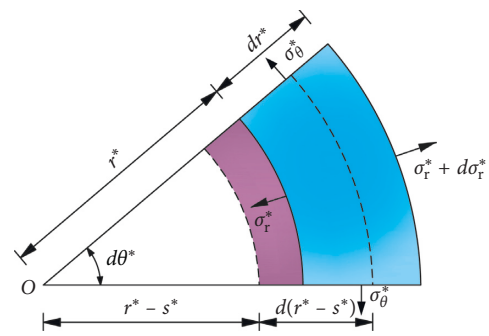

Figure 6: Force and displacement of cylindrical cavity microelement.

$$s^* = r^*\left[1 - \left(1 - \frac{(r_q^*)^2}{(r^*)^2}\right)^{1/2}\right], \tag{55}$$

where r_q^* is the radius of the cylindrical cavity.

Substituting equation (55) in equation (51), and given that the radius of the plastic zone of the soil cushion layer r_q^* is far less than the radius of elastic zone r^*, we obtain

$$\varepsilon_r^* - \varepsilon_\theta^* = \left(\frac{r_q^*}{r^*}\right)^2\left[1 - \left(\frac{r_q^*}{r^*}\right)^2\right]^{-(1/2)} \approx \left(\frac{r_q^*}{r^*}\right)^2. \tag{56}$$

Combining equations (56) and (52), we obtain

$$\sigma_r^* - \sigma_\theta^* = \frac{E}{(1+v)}\left(\frac{r_q^*}{r^*}\right)^2. \tag{57}$$

Substituting equation (57) in (50) and considering the boundary conditions $r^* \longrightarrow \infty$ and $\sigma_r^* = 0$, we obtain

$$\sigma_r^* = \frac{E}{(1+v)}\left(\frac{r_q^*}{r^*}\right)^2. \tag{58}$$

Assuming the soil cushion layer is an ideal elastic-plastic body, we obtain the failure criterion according to equation (59):

$$\sigma_r^* - \sigma_\theta^* = 2\tau_0 = \sigma_y. \tag{59}$$

Substituting equation (59) into (50), we obtain

$$\frac{\partial \sigma_r^*}{\partial r^*} + \frac{2\tau_0}{r^*} = 0. \tag{60}$$

Further, consider the boundary conditions $r^* = r_p^*$, $\sigma_r^* = \sigma_{rq}^*$, we obtain

$$\sigma_r^* = \sigma_{rq}^* + 2\tau_0 \ln\left(\frac{r_q^*}{r^*}\right), \tag{61}$$

where σ_{rq}^* is the radial stress on the cylindrical cavity surface.

According to the boundary conditions $r^* = r_p^*$ and $\sigma_{rq}^{*-} = \sigma_{rq}^{*+}$ for the assumption of a continuous medium in the elastic-plastic zone and combined with the yield criterion of equation (59), we obtain t equation (62) for the surface stress of a cylindrical cavity:

$$\sigma_{rq}^* = \tau_0 \ln\left[\frac{eE}{2\tau_0(1+\upsilon)}\right], \tag{62}$$

where σ_p^* is the plastic region radius of cylindrical cavity.

4.2. Energy Dissipation due to Crater Formation. Using the slices method, the energy dissipation due to crater formation is equal to the sum of energy works of the surface stress of each cylindrical cavity in the stripe microbody, as shown in Figure 7.

$$W_e = \int_0^{r_{qf}^*} 2\pi r_q^* \sigma_{rq}^* dr_q^* = \pi \sigma_{rq}^* \left(r_{qf}^*\right)^2, \tag{63}$$

where x^* and y^* are expressed by the equations below:

$$\begin{cases} r_{qf}^* = x^*, \\ y^* = R - \sqrt{R^2 - (x^*)^2}, \end{cases} \tag{64}$$

where x^* is the x coordinate value of point G^* on the rockfall surface and y^* is the y coordinate value of point G^* on the rockfall surface.

Substitute equation (64) into (63), we obtain

$$W_e = \pi\tau_0\left[2Ry^* - (y^*)^2\right] \ln\left[\frac{eE}{2\tau_0(1+\upsilon)}\right]. \tag{65}$$

Using the above equations, we can obtain the final energy dissipation due to crater formation of the rockfall:

$$\begin{aligned} W_{te} &= \int_0^{L_{max}^*} W_e \, dz \\ &= \int_0^{L_{max}^*} \pi\tau_0\left[2Ry^* - (y^*)^2\right] \ln\left[\frac{eE}{2\tau_0(1+\upsilon)}\right] dy^*, \end{aligned} \tag{66}$$

where W_e is the energy dissipated due to the deformation of thin layer of soil cushion layer, W_{te} is the total energy dissipated due to the deformation of soil cushion layer, and L_{max}^* is the maximum penetration depth of the rockfall by energy method.

4.3. Energy Dissipation due to Friction. Combined with Figures 7 and 8, the slices method is adopted to analyze the internal energy dissipation due to the friction of rockfall and soil cushion layer.

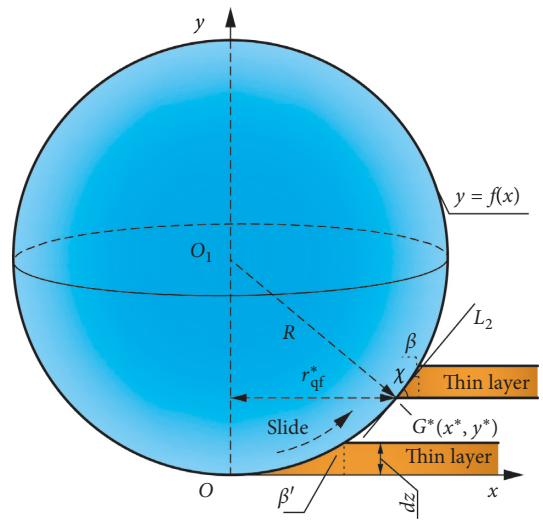

Figure 7: Relative displacement diagram of thin layer.

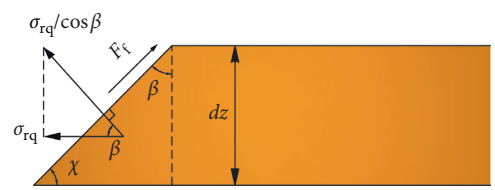

Figure 8: Stress analysis of thin layer.

In Figure 9, the friction of thin layer of microsoil cushion layer and rockfall F_f is

$$F_f = \frac{2\pi r_q^* \mu \sigma_{rq}^*}{\cos\beta}, \tag{67}$$

where F_f is the friction between the thin layer of soil cushion layer and the rockfall, μ is the friction coefficient between soil cushion layer and the rockfall, and β is the acute angle between the inclined plane of the thin soil layer with the vertical line.

Combined with Figure 7, when the thin layer of soil cushion layer has the displacement r_{qf}^* relative to rockfall, the energy work of friction F_f is

$$W_{hf} = 2\pi\mu \int_0^{r_{qf}^*} r_q^* \sigma_{rq}^* \frac{dz}{\cos^2\beta}, \tag{68}$$

where r_{qf}^* is the horizontal movement distance of the thin soil layer, dz is the thickness of the soil layer and W_{hf} is the energy dissipated due to friction between the rockfall and the soil cushion layer.

Further, the expression for the side profile of rockfall is

$$z = f\left(r_q^*\right) dr_q^*. \tag{69}$$

Combining equations (62), (68), and (69), we obtain

$$W_{hf} = 2\pi\mu\tau_0 \ln\left[\frac{eE}{2\tau_0(1+\upsilon)}\right] \int_0^{r_{qf}^*} r_q^* f'\left(r_q^*\right) \frac{dr_q^*}{\cos^2\beta}. \tag{70}$$

In equation (70), dr_q^* is the distance of movement of a thin layer of soil cushion relative to the rockfall. This can be determined using equation (71):

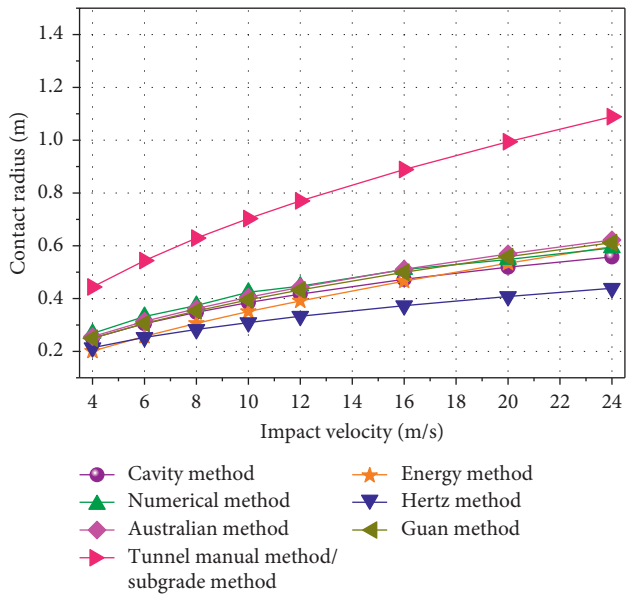

Figure 9: "Impact velocity-contact radius" curve.

$$dy^* = \frac{x^*}{\sqrt{R^2 - (x^*)^2}} dx^*. \tag{71}$$

To determine $\cos\beta$ as represented in Figure 7, a tangent line L_2 is made through the contact point of the thin layer of soil cushion and rockfall and the included angle of L_2. The horizontal axis is β, so we obtain

$$y_2' = \tan\chi, \tag{72}$$

where y_2' is the slope of the tangent line L_2 and χ is the acute angle between the inclined plane of the thin soil layer with the horizontal line.

Further, based on the trigonometric function relation,

$$\begin{cases} \sec^2\chi - 1 = \tan^2\chi, \\ \sec\chi = \cos^{-1}\chi, \end{cases} \tag{73}$$

and combining the equations (72) and (73), we obtain

$$\cos\chi = \frac{1}{\sqrt{1 + (y_2')^2}}. \tag{74}$$

Combining equations (71) and (72), we obtain

$$y_2' = \frac{dy^*}{dx^*} = \frac{x^*}{\sqrt{R^2 - (x^*)^2}}. \tag{75}$$

Combining equations (74) and (75), we obtain

$$\sin^2\chi = \frac{(x^*)^2}{R^2}. \tag{76}$$

According to Figure 8, we can write the equation (77):

$$\chi + \beta = \frac{\pi}{2}, \tag{77}$$

and we can state that

$$\cos^2\beta = \frac{(x^*)^2}{R^2}. \tag{78}$$

According to the above equations, we obtain the final expression of equation (79):

$$W_{hf} = 2\pi R^2 \mu \tau_0 \left(\arcsin \frac{\sqrt{2Ry^* - (y^*)^2}}{R} \right) \ln\left[\frac{eE}{2\tau_0 (1 + v)} \right]. \tag{79}$$

Therefore, when rockfall has the maximum penetration depth of L^*_{max}, the energy dissipation due to friction is

$$W_{th} = \int_0^{L^*_{max}} W_{hf}\, dy^*, \tag{80}$$

where W_{th} is the total energy dissipated due to friction between the rockfall and the soil cushion layer.

4.4. Energy Dissipation of Shed Tunnel Structure. Under the impact effect of rockfall load, the roof of a shed tunnel structure will have slight deflection deformation due to rockfall impact, and therefore, energy is dissipated. The deflection of the roof of the shed tunnel under an impact force P_f is [39]

$$\delta_f = \frac{P_f (l^*)^3}{48 E_1 I}, \tag{81}$$

where δ_f is the roof deflection of the shed tunnel structure, P_f is the Given rockfall impact load, E_1 is the elasticity modulus of the roof of the shed tunnel structure, I is the inertia moment of the roof of the shed tunnel structure, and l^* is the span of the shed tunnel structure.

According to structural mechanics and equation (81), we obtain the relevant energy of deformation as

$$W_f = \frac{P_f^2 (l^*)^3}{96 E_1 I}. \tag{82}$$

Further, W_f can be determined using equation (83):

$$W_f = \frac{\pi^2 \sigma_y^2 \left(2RL_{max} - (L^*_{max})^2\right)^2 (l^*)^3}{96 E_1 I}, \tag{83}$$

where σ_y is the yield strength of soil cushion layer and W_f is the total energy dissipated due to the deflection deformation of the roof of the shed tunnel.

4.5. Penetration Depth. The initial kinetic energy of rockfall during the impact process is $Mv_0^2/2$; the energy of deformation due to crater W_{te} shall be calculated using equation (66), the energy of friction W_{th} using equation (80), and the energy of deflection deformation of the roof of the shed tunnel W_f using equation (83). The work done by gravity during rockfall impact process is MgL^*_{max}; therefore, according to the law of energy conservation, we obtain:

$$\frac{Mv_0^2}{2} = W_{te} + W_{th} + W_f - MgL^*_{max}. \tag{84}$$

There is only one unknown parameter $L^*_{\max}$ in equation (76), so we obtain the solution using equation (84). The value of the impact force F is obtained based on $L^*_{\max}$.

4.6. Impact Force. According to the principle of work and energy, the relation expression during the contact of the rockfall and the soil cushion layer is

$$F^*_a \cdot L^*_{\max} = \frac{Mv_0^2}{2} + MgL^*_{\max}, \tag{85}$$

where F^*_a is the average impact force of rockfall.

The F^*_a value determined using equation (85) is the average of the impact force. However, the rockfall impact process is an impulse type, Yang et al. [37], and with the vibration curve of the impact force over time during the impact process that simulates the process of changes of impact force approximately in the form of a sine function, we obtain

$$F = F^*_{\max} \sin(\omega_0 t_1), \tag{86}$$

where $F^*_{\max}$ is the maximum impact force of the rockfall, ω_0 is the angular frequency, and t_1 is the time.

Since the impulse due to actual impact force is equal to that of the average impact force of rockfall, we obtain equation (87):

$$F^*_a \cdot t_w = \int_0^{t_w} F(t_1)\, dt_1. \tag{87}$$

Combining the equations (86) and (87), we obtain

$$F^*_a = \frac{\int_0^{t_w} F^*_{\max} \sin(\pi t_1/t_w)\, dt_1}{t_w}. \tag{88}$$

Further, we have

$$F^*_{\max} = \frac{\pi F^*_a}{2}, \tag{89}$$

and the time duration of rockfall impact is

$$t_w = \frac{2Mv_0}{F^*_a}. \tag{90}$$

5. LS-DYA Numerical Simulation Analysis

In order to evaluate the theoretical calculation result and explore the detailed process of rockfall impacting on the soil cushion layer, LS-DYA software was used to analyze the impact process. A typical working condition is taken as an example: size of the soil cushion layer is 6 m (length) × 6 m (width) × 3 m (height); the radius of the rockfall is 0.5 m; and impact velocity of rockfall is 20 m/s. Face-to-face contact is set between the rockfall and the soil cushion layer, and grid refinement is conducted within the range of 1.5 m × 1.5 m in the center of the soil cushion layer. All the nodes in the bottom of the cushion are restricted in three directions: 0.06 s is set as the total time of the analysis step and 200 steps are chosen as the total calculation steps. The calculation parameters are shown in Tables 1 and 2.

Table 1: Slope soil parameters of the calculation model.

Volume-weight (kN/m^3)	Elasticity modulus (MPa)	Poisson's ratio	Yield strength (kPa)	Friction coefficient of rock and soil
20.5	40	0.3	400	0.4

Figure 10 shows the results of the LS-DYNA numerical model and the numerical simulation results at 0.02 s, 0.04 s, and 0.06 s. Figure 11 shows the variation curves of impact force and penetration depth of the rockfall with time. After rockfall impact on soil cushion layer, the impact force of the rockfall reaches a maximum value of 1559801 N at 0.004 s (14/200 steps), then reduces gradually, and finally reaches a value of 0 at 0.44 s (147/200 steps). However, the curve shows a stronger vibration between 0.018 s and 0.026 s. The penetration depth of the rockfall gradually increases in the range 0~0.035 s and reaches a maximum value 0.35 m at 0.035 s (117/200 step), but approximately 9% spring back quantity is generated between 0.035 s and 0.05 s, forming the ultimate penetration depth of 0.312 m.

6. Engineering Example

6.1. Influence of Rockfall Velocity. We have investigated the effects of the collisions of a rockfall block, 0.5 m in radius, with the soil cushion layer when the impact speed of the block is 4, 6, 8, 10, 12, 16, 20, and 24 m/s.

6.1.1. "Impact Velocity-Penetration Depth" Relation Analysis. Figure 12 shows the plot of "impact velocity vs penetration depth." With an increase in the rockfall impact velocity, the results of these eight methods all reveal a trend of linear growth. The calculation results for the rockfall penetration depth obtained using the cavity expansion, energy conservation, numerical simulation, Australian, and B. S. Guan methods all demonstrated good consistency. Comparatively, the Hertz method has smaller results, while the results from the tunnel manual method and subgrade method are obviously larger.

6.1.2. "Impact Velocity-Contact Radius" Relation Analysis. Figure 9 shows a plot of "impact velocity vs contact radius." The "contact radius" in this study is defined as follows: when a rock falls on the earth, there is a certain contact area between them. The contact area is calculated and converted into an equivalent circle, and the radius of the circle is the contact radius. From Figure 9, the variation trend for the results of the eight methods is basically consistent with that in Figure 12. In addition, the calculation results for the contact radius based on the cavity expansion, energy conservation, numerical simulation, Australia, and B. S. Guan methods reveal better consistency.

6.1.3. "Impact Velocity vs Impact Force" Relation Analysis. Figure 13 represents the plot of "Impact velocity vs impact force." With the increase in rockfall impact velocity, the calculation results for the 10 methods all reveal a linear growth trend. The calculation results for the cavity

Table 2: Rockfall and shed tunnel beam parameters of the calculation model.

Rockfall				Shed tunnel beam			
Volume-weight (kN/m^3)	Elasticity modulus (MPa)	Radius (m)	Falling height (m)	Elasticity modulus (MPa)	Poisson's ratio	Profile moments of inertia (m^4)	Span (m)
25	28	0.5	20	28.5	0.19	0.057	10

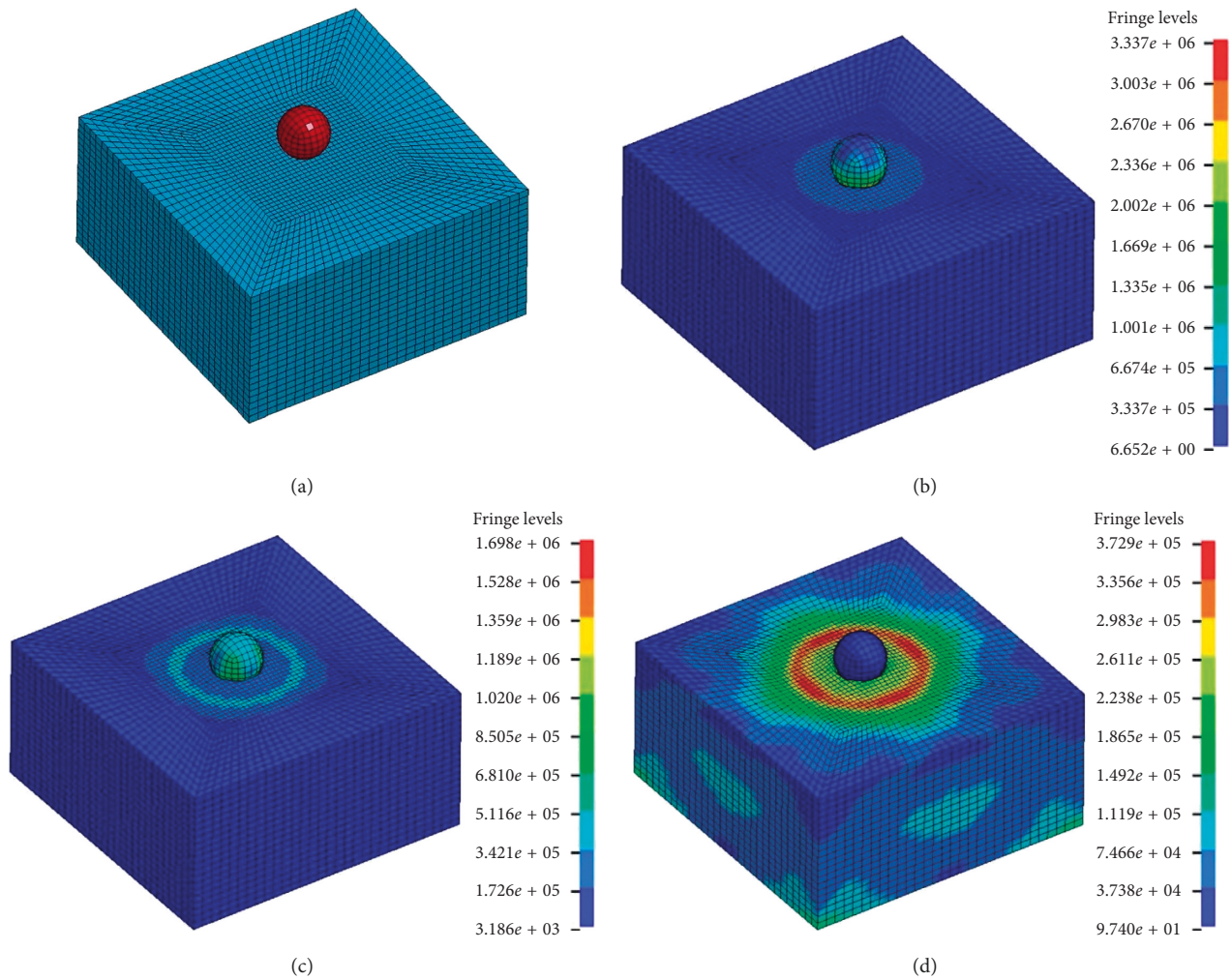

Figure 10: Numerical model and results.

expansion, energy conservation, numerical simulation, Japanese, Swiss, and Australian methods demonstrate better consistency. In contrast, the calculation results for the B. S. Guan, tunnel manual, and subgrade methods are smaller overall, while the calculation result for the Hertz method is slightly larger.

6.1.4. "Penetration Depth-Impact Force" Relation Analysis. Figure 14 shows the curve of "penetration depth vs impact force." The difference between the curves for the eight methods is evident. The calculation results based on the cavity expansion, energy conservation, numerical simulation, and Australian methods demonstrate better consistency. In comparison, the B. S. Guan method exhibited a slightly smaller impact force with an appropriate penetration depth, the tunnel manual method, and subgrade method exhibited weaker impact forces with larger penetration depth, while the Hertz Method resulted in a greater force with a smaller penetration depth.

6.1.5. "Contact Radius vs Impact Force" Relation Analysis. Figure 15 shows the curve for the "contact radius vs impact force." According to the figure, the difference between the plots for the eight methods is basically the same as that of Figure 14. The calculation results for the cavity expansion, energy conservation, numerical simulation, and Australian methods demonstrated better consistency and moderate positions.

6.2. Influence of Rockfall Radius. The impact velocity of 20 m/s and rockfall radii of 0.2 m, 0.3 m, 0.4 m, 0.5 m, 0.6 m,

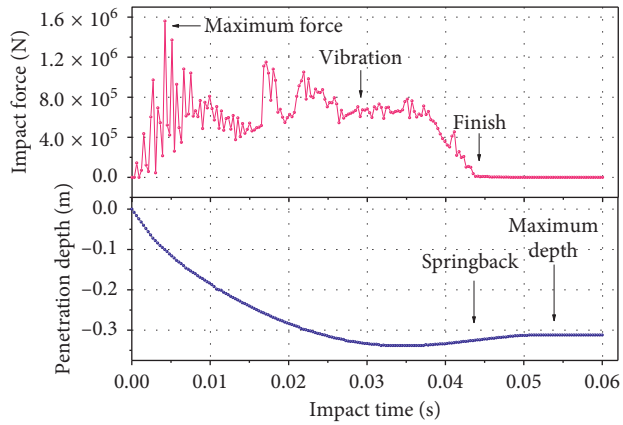

Figure 11: Impact force and penetration depth of simulation.

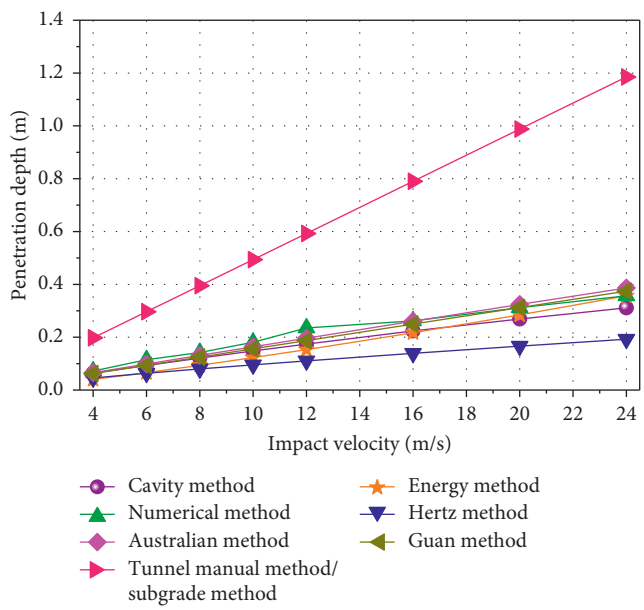

Figure 12: "Impact velocity-penetration depth" curve.

0.7 m, and 0.8 m were considered to analyze the impact effect of rockfall on the soil cushion layer.

6.2.1. "Rockfall Radius vs Penetration Depth" Relation Analysis. Figure 16 shows the curve of "rockfall radius vs penetration depth." The calculation results for the eight methods all reveal linear growth trends. The calculation results for the penetration depth based on the cavity expansion, energy conservation, numerical simulation, Australian, and B. S. Guan methods demonstrated better consistency. In contrast, the results for the Hertz method are smaller, while that of the tunnel manual method and subgrade method are obviously larger.

6.2.2. "Rockfall Radius vs Impact Force" Relation Analysis. Figure 17 represents the curve of "rockfall radius vs impact force." According to Figure 17, with the increase in the rockfall radius, the calculation results for the 10 methods all

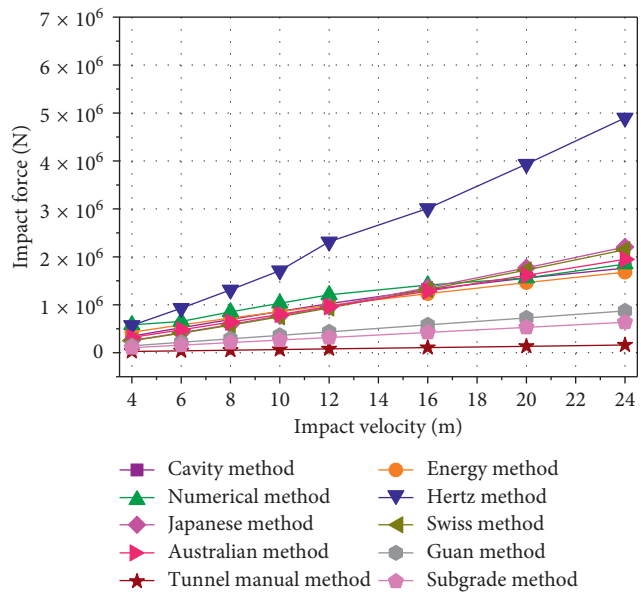

Figure 13: "Impact velocity vs impact force" curve.

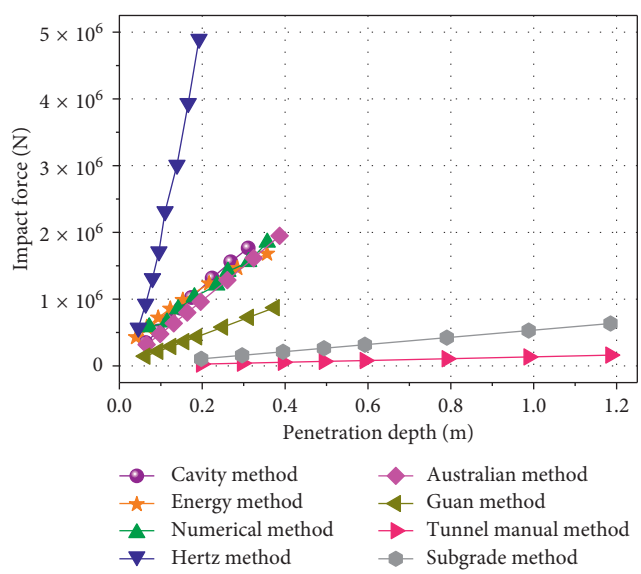

Figure 14: "Penetration depth vs impact force" curve.

reveal a linear growth trend. The calculation results for the cavity expansion, energy conservation, numerical simulation, Japanese, Swiss, and Australian methods demonstrated better consistency, while the calculation results for the B. S. Guan, tunnel manual, and subgrade methods are all smaller. In addition, the calculation result for the Hertz method is slightly larger.

6.2.3. "Rockfall Radius vs Contact Radius" Relation Analysis. Figure 18 shows the curve of "rolling stone radius vs contact radius." As shown in this figure, the variation trend of the results for the 8 methods is basically consistent with that shown in Figure 7. Moreover, the calculation results for the contact radius obtained using the cavity expansion, energy

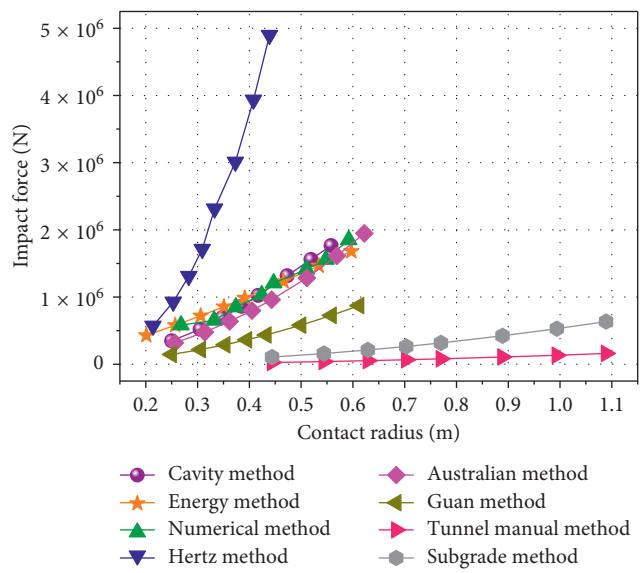

Figure 15: "Contact radius-impact force" curve.

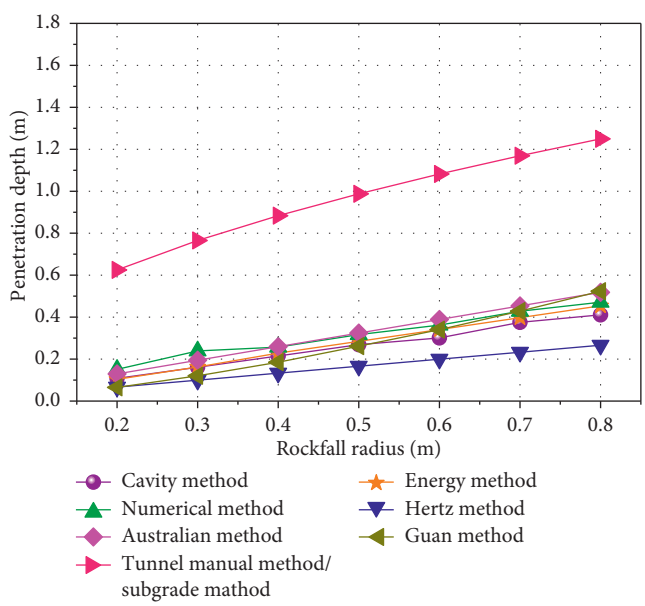

Figure 16: "Rockfall radius-penetration depth" curve.

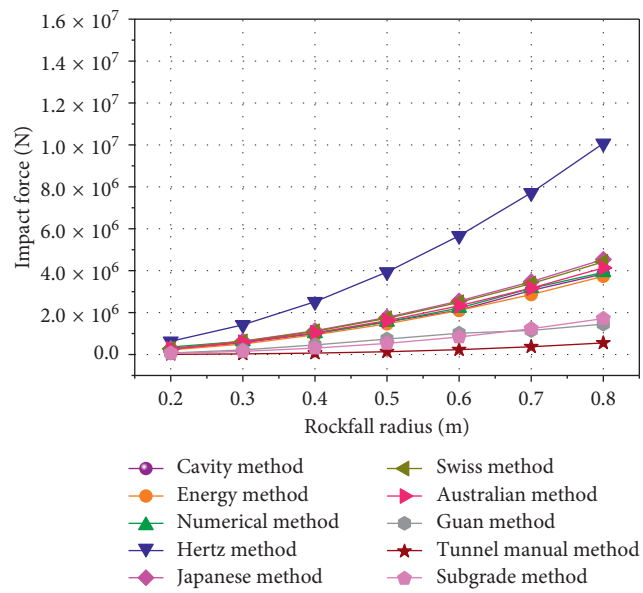

Figure 17: "Rockfall radius vs impact force" curve.

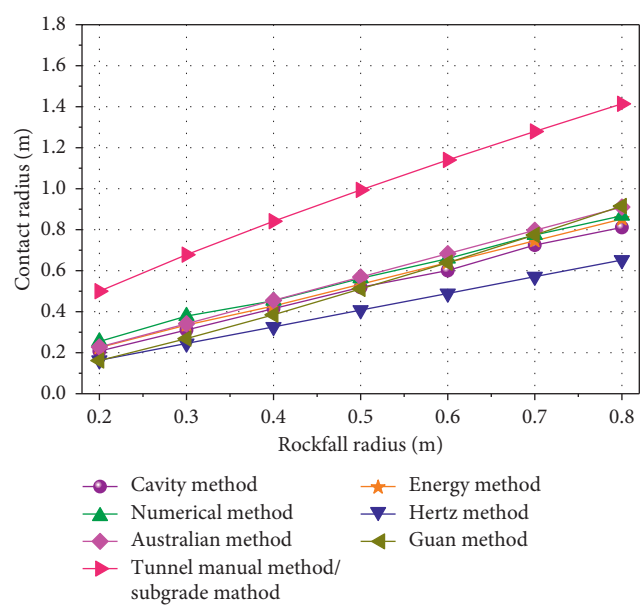

Figure 18: "penetration depth vs impact force" curve.

conservation, Australian, numerical simulation, and B. S. Guan methods are relatively consistent.

As observed from the preceding analysis, the calculation results for the rockfall impact force and penetration depth based on the cavity expansion, energy conservation, numerical simulation, Japanese, Swiss, and Australian methods reveal better consistency, which explains why the cavity expansion method and energy conservation method have better accuracy. In comparison, the penetration depth obtained for the B. S. Guan method is accurate, but the impact force is slightly smaller. The calculation results for the impact force obtained using the tunnel manual method and subgrade method are smaller, while the calculation result for the penetration depth is larger. In addition, the calculation results for the penetration depth based on the Hertz method are smaller, while that of the impact force is larger.

6.3. Energy Dissipation Analysis

6.3.1. Analysis on Impact Velocity Influence on Energy Dissipation of Rockfall. We analyzed the energy dissipation of the rockfall impact with the rockfall radius of 0.5 m and impact velocity of 4, 6, 8, 10, 12, 16, 20, and 24 m/s.

Figure 19 represents the "influence of impact velocity on energy dissipation", from which it can be seen that with an increase in the impact velocity, the energy dissipation due to crater formation and due to friction increase rapidly. The increase rate and tendency of the two curves are basically

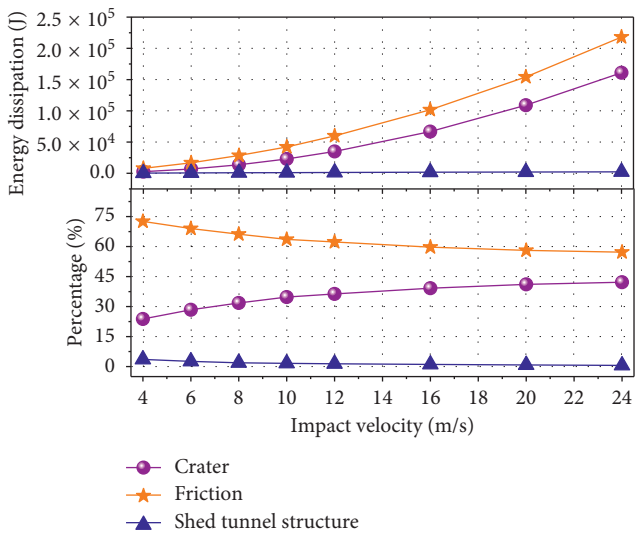

Figure 19: Influence of impact velocity on energy dissipation.

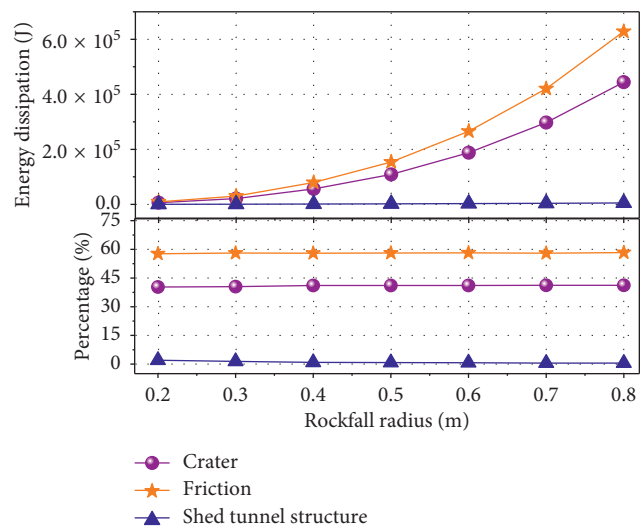

Figure 20: Influence of rockfall radius on energy dissipation.

consistent. Furthermore, the gross energy dissipation due to friction is always higher than that due to crater formation, and the energy dissipation of the shed tunnel structure is small overall. Figure 19 also shows the proportion of three kinds of energy dissipations under impact velocity, from which it can be seen that the proportion of energy dissipation due to crater formation gradually rises from approximately 25% to approximately 40% and then becomes stable. Energy dissipation due to friction decreases from approximately 70% to 60% and becomes stable. The energy dissipation of the shed tunnel structure also decreased from approximately 5% to approximately 0%. Therefore, the energy dissipation of the shed tunnel structure could be ignored.

6.3.2. Analysis on the Influence of the Rockfall Radius on Energy Dissipation. Futher, the impact velocity of 20 m/s and rockfall radii of 0.2 m, 0.3 m, 0.4 m, 0.5 m, 0.6 m, 0.7 m, and 0.8 m were considered to analyze the energy dissipation of the rockfall impact.

Figure 20 represents the "Influence of rockfall radius on energy dissipation." Based on this figure, it can be seen that the energy dissipation due to crater formation and friction increases rapidly with an increase in the rockfall radius. In addition, the increasing tendency of the two curves is consistent. Furthermore, energy dissipation due to friction is always higher than that due to crater formation. Figure 20 also shows the proportion of energy dissipation for different rockfall radii. It can be seen that energy dissipation due to crater formation is maintained at approximately 40% and that friction is approximately 60%, which further indicates that the energy dissipation of a conventional shed tunnel structure can be ignored.

7. Conclusion

In this study, the impact force and penetration depth of rockfall were analyzed theoretically. The main conclusions are as follows:

(1) This investigation began with an analysis of the mechanical response mechanism of rockfall impact on the soil cushion layer. Based on the theoretical derivation and the combined cavity expansion model and energy conservation model, respectively, two analytical solutions for the penetration depth and impact forces were obtained. Further, the LS-DYNA software was employed to study the variation law of penetration depth and impact force.

(2) For the impact force of the rockfall, either with the change of impact velocity or its radius, the calculation results for the cavity expansion, energy conservation, and numerical simulation methods demonstrated better consistency and coincided well with the results for the Japanese, Swiss, and Australian methods. The results of the Japanese method and the Swiss method were obtained based on laboratory tests. The results for the Australian method were acquired based on field tests.

(3) For the penetration depth and contact radius of the rockfall either with the change of impact velocity or its radius, the calculation results for the cavity expansion, energy conservation, numerical simulation, and B. S. Guan methods exhibited better consistency and coincided well with the results for the Australia method.

(4) For the relation between the "penetration depth-impact force" and the "contact radius-impact force," the calculation results for the cavity expansion, energy conservation, numerical simulation, and Australian methods exhibited better consistency. The penetration depth obtained using the Hertz Method was smaller, and the value for the impact force was greater. In comparison, the tunnel manual method and ubgrade method showed inverse results. The penetration depth obtained using the B. S. Guan method is accurate, but the impact force is slightly smaller. Thus, this indicates that the cavity expansion

method and energy conservation method have better accuracy.

(5) When the impact velocity or radius of the rockfall increases, both the deformation energy consumption and friction energy consumption increase in the form of a parabola. Further, the friction energy consumption is a bit larger than the deformation energy consumption. The impact velocity of the rockfall will influence the energy dissipation ratio for various energies, while the radius of the rockfall has a slight influence. A normal shed hole structure rarely influences the energy dissipation process.

Notations

σ_A: Normal stress at point A of soil cushion layer
$\sigma_{\mathrm{rq}(A)}$: Normal stress at point A of spherical cavity
$r_{\mathrm{q}}(A)$: Radius of the spherical cavity
x_A: The x coordinate value of point A
α: The acute angle between the normal line and the vertical line at point A
v_{h}: The velocity of rockfall impact
$\dot{v}_{\mathrm{h}}$: The acceleration of a rockfall impact
v_{q}: The velocity of spherical cavity expansion
$\dot{v}_{\mathrm{q}}$: The acceleration of spherical cavity expansion
r_{q}: Radius of spherical cavity
r_{q}^*: Radius of the cylindrical cavity
$\dot{r}_{\mathrm{q}}$: The expansion velocity of spherical cavity
$\ddot{r}_{\mathrm{q}}$: The expansion acceleration of spherical cavity
θ: The opening angle of spherical cavity microbody
θ^*: The opening angle of cylindrical cavity microbody
ρ_0: The density before deformation of spherical cavity microbody
ρ_0^*: The density before deformation of cylindrical cavity microbody
ρ: The density after deformation of spherical cavity microbody
ρ^*: The density after deformation of cylindrical cavity microbody
r: Distance from the coordinate origin to the mass point of the spherical cavity microbody
r^*: Distance from the coordinate origin to the mass point of the cylindrical cavity microbody
s: The displacement of the mass point of the spherical cavity microbody
s^*: The displacement of the mass point of the cylindrical cavity microbody
v: Moving velocity of the mass point of the spherical cavity microbody
t: Moving time of the mass point of the spherical cavity microbody
σ_{r}: The radial stress of the spherical cavity microbody
σ_{r}^*: The radial stress of the cylindrical cavity microbody
σ_θ: The hoop stress of the spherical cavity microbody
σ_θ^*: The hoop stress of the cylindrical cavity microbody
ε_{r}: The radial strain of spherical cavity microbody
$\varepsilon_{\mathrm{r}}^*$: The radial strain of cylindrical cavity microbody
ε_θ: The hoop strain of spherical cavity microbody
ε_θ^*: The hoop strain of cylindrical cavity microbody
r_{p}: The plastic region radius of spherical cavity
r_{p}^*: The plastic region radius of cylindrical cavity
v: Poisson's ratio of soil cushion layer
E: Elasticity modulus of soil cushion layer
τ_0: The shear strength of soil cushion layer
τ: The undrained shear strength of soil cushion layer
K: Shear strength coefficient of soil cushion layer
σ_{rq}: Radial stress on the spherical cavity surface
σ_{rq}^*: Radial stress on the cylindrical cavity surface
φ: The acute angle between the tangent at the spherical cavity surface through point M with x axis
x: x coordinate value of point G on spherical cavity
y: y coordinate value of point G on spherical cavity
x^*: x coordinate value of point G^* on the rockfall surface
y^*: y coordinate value of point G^* on the rockfall surface
y_1': The slope of the tangent line L_1
y_2': The slope of the tangent line L_2
R_1: Radius of the horizontal infinitesimal cavity at the upper surface of soil cushion layer
l: The width value of infinitesimal cavity
R: The radius of the rockfall block
D: The diameter of the rockfall block
M: Mass of the rockfall block
L: The penetration depth of the rockfall impact
$L_{\max}$: Maximum penetration depth of the rockfall by cavity method
$L_{\max}^*$: Maximum penetration depth of the rockfall by energy method
F, F_1, F_2: Rockfall impact force
F_{a}^*: Average impact force of rockfall
$F_{\max}^*$: The maximum impact force of the rockfall
σ_{y}: Yield strength of soil cushion layer
r_{qf}^*: The horizontal movement distance of the thin soil layer
β: The acute angle between the inclined plane of the thin soil layer with the vertical line
dz: Thickness of the soil layer
χ: The acute angle between the inclined plane of the thin soil layer with the horizontal line
W_{e}: The energy dissipated due to the deformation of thin layer of soil cushion layer
W_{te}: The total energy dissipated due to the deformation of soil cushion layer
F_{f}: The friction between the thin layer of soil cushion layer and the rockfall
μ: The friction coefficient between soil cushion layer and the rockfall
W_{hf}: The energy dissipated due to friction between the rockfall and the soil cushion layer
W_{th}: The total energy dissipated due to friction between the rockfall and the soil cushion layer
W_{f}: The energy dissipated due to the deflection deformation of the roof of the shed tunnel structure
δ_{f}: The roof deflection of the shed tunnel structure

P_f: Given rockfall impact load
E_1: Elasticity modulus of the roof of the shed tunnel structure
I: The inertia moment of the roof of the shed tunnel structure
l^*: Span of the shed tunnel structure
ω_0: Angular frequency
t_1: Time
Q: Quality of rockfall block
M_E: The deformation modulus of soil cushion layer
H: Falling height of the rockfall block
v_0: The initial velocity of the rockfall block
λ: Lame constants
V: Volume of the rockfall block
R_c: Indentation resistance of target materials
h: The thickness of soil cushion layer
t_w: The impact time of the rockfall
c: The reciprocating velocity of compression waves in the soil cushion layer
γ: The specific gravity of the soil cushion layer
ψ: The cross-sectional area of an equivalent sphere for rockfall
ζ: The correction coefficient of the rockfall impact force
κ: The coefficient of rockfall penetration depth
g: Gravitational acceleration
a: The acceleration of the rockfall impact
φ^*: Inner friction angle of soil cushion layer.

Data Availability

The data used to support the findings of this study are available from the corresponding author upon request.

Conflicts of Interest

The authors declare that there are no conflicts of interest regarding the publication of this article.

Acknowledgments

This work was made possible by the Sichuan Provincial Traffic Construction Science and Technology Project (2015A1-3) and Fundamental Research Funds for the Central Universities (no. 310826151048). The two sources of financial support are highly appreciated.

References

[1] G. Qin, S. Cao, and F. Yang, "Effect of deficiencies in the tunnel crown thickness on pressure tunnels with post-tensioned concrete linings," *Advances in Civil Engineering*, vol. 2018, Article ID 2757542, 14 pages, 2018.

[2] Y. Zhou, Y. Wu, Z. Shangguan, and Z. Wang, "Effects of spatially varying seismic ground motions and incident angles on behavior of long tunnels," *Advances in Civil Engineering*, vol. 2018, Article ID 8195396, 16 pages, 2018.

[3] H. Chen and C. Sha, "Stability analysis of surrounding rock and treatment structures in superlarge Karst cave of Naqiu tunnel," *Advances in Civil Engineering*, vol. 2018, Article ID 4842308, 14 pages, 2018.

[4] S. Z. Song and J. M. Kong, "Analysis of rockfall and its impact on the cut-and-cover tunnel in dynamics," *Wuhan University Journal of Nature Sciences*, vol. 11, no. 4, pp. 905–909, 2006.

[5] C. Thornton, "Coefficient of restitution for collinear collisions of elastic-perfectly plastic spheres," *Journal of Applied Mechanics*, vol. 64, no. 2, p. 383, 1997.

[6] C. Thornton and Z. Ning, "A theoretical model for the stick/bounce behaviour of adhesive, elastic-plastic spheres," *Powder Technology*, vol. 99, no. 2, pp. 154–162, 1998.

[7] B. Pichler and C. Hellmich, "Impact of rocks onto gravel design and evaluation of experiments," *International Journal of Impact Engineering*, vol. 31, no. 5, pp. 59–578, 2005.

[8] B. Cagnoli and M. Manga, "Pumice-pumice collisions and the effect of the impact angle," *Geophysical Research Letters*, vol. 30, no. 12, pp. 53–62, 2003.

[9] K. L. Johnson, *Contact Mechanics*, Cambridge University Press, Cambridge, UK, 1985.

[10] V. Labiouse, F. Descoeudres, and S. Montani, "Experimental study of rock sheds impacted by rock blocks," *Structural Engineering International*, vol. 6, no. 3, pp. 171–176, 2018.

[11] N. Kishi and K. Ikeda, "Prototype impact test on rockfall retaining walls and its numerical simulation," *Materials and Structures*, vol. 8, pp. 351–360, 2000.

[12] B. Heidenreich and V. Labiouse, *Small-Scale Experimental Studies of Rockfall Impacts on Granular Slopes*, Rivista Italiana di Geotecnica, Italy, 2004.

[13] F. Calvetti and C. D. Prisco, *Experimental and Numerical Study of Rock-Fall Impacts on Granular Soils*, Rivista Italiana di Geotecnic, Vol. 4, Rivista Italiana di Geotecnic, Italy, 2005.

[14] J.-P. Mougin, P. Perrotin, M. Mommessin, J. Tonnelo, and A. Agbossou, "Rock fall impact on reinforced concrete slab: an experimental approach," *International Journal of Impact Engineering*, vol. 31, no. 2, pp. 169–183, 2005.

[15] F. Delhomme, M. Mommessin, J. P. Mougin, and P. Perrotin, "Behavior of a structurally dissipating rock-shed: experimental analysis and study of punching effects," *International Journal of Solids and Structures*, vol. 42, no. 14, pp. 4204–4219, 2005.

[16] S. Kawahara and T. Muro, "Effects of dry density and thickness of sandy soil on impact response due to rockfall," *Journal of Terramechanics*, vol. 43, no. 3, pp. 329–340, 2006.

[17] F. Calvetti and C. D. Prisco, "An uncoupled approach for the design of rockfall protection tunnels," *Structural Engineering International*, vol. 19, no. 3, pp. 342–347, 2018.

[18] S. Q. Ye and H. K. Chen, "Comparative research on impact force calculation methods for rockfalls," *Hydrogeology and Engineering Geology*, vol. 37, no. 2, pp. 59–64, 2010.

[19] S. Q. Ye, K. Li, and H. K. Chen, "Numerical simulation of rockfall impact force in the case of oblique impacting," in *Proceedings of International Conference on Electric Technology and Civil Engineering (ICETCE)*, Lushan, China, April 2011.

[20] S. Qi, C. Zhou, S. H. Liu, and X. Song, "Study on impact force of landfall and rockfall," *Applied Mechanics and Materials*, vol. 256–259, pp. 81–85, 2012.

[21] J. K. Yuan, Y. R. Li, R. Q. Huang, and X. J. Pei, "Impact of rockfalls on protection measures: an experimental approach," *Natural Hazards and Earth System Sciences*, vol. 15, no. 1, pp. 885–893, 2015.

[22] J. Sun, Z. Chu, Y. Liu, W. Luo, and M. Wang, "Performance of used tire cushion layer under rockfall impact," *Shock and Vibration*, vol. 2016, Article ID 8760592, 10 pages, 2016.

[23] J. Zhang, Z. Liang, and C. Han, "Numerical simulation of pipeline deformation caused by rockfall impact," *The Scientific World Journal*, vol. 2014, Article ID 161898, 10 pages, 2014.

[24] J. Hu, S. Li, S. Shi et al., "Experimental study on parameters affecting the Runout range of rockfall," *Advances in Civil Engineering*, vol. 2018, Article ID 4739092, 9 pages, 2018.
[25] C. Lam, A. C. Y. Yong, J. S. H. Kwan, and N. T. K. Lam, "Overturning stability of L-shaped rigid barriers subjected to rockfall impacts," *Landslides*, vol. 15, no. 7, pp. 1347–1357, 2018.
[26] M. Basharat, M. Kashif, and Y. Sarfraz, "Effects of volume and topographic parameters on rockfall travel distance: a case study from NW Himalayas, Pakistan," *Quarterly Journal of Engineering Geology and Hydrogeology*, vol. 51, no. 3, pp. 387–398, 2018.
[27] C. Zhu, D. Wang, X. Xia, Z. Tao, M. He, and C. Cao, "The effects of gravel cushion particle size and thickness on the coefficient of restitution in rockfall impacts," *Natural Hazards and Earth System Sciences*, vol. 18, no. 6, pp. 1811–1823, 2018.
[28] F.-j. Luo, X.-j. Zhou, Y. Wang, and F.-l. Zhang, "Experimental study on rockfall impact force applied to frame shed tunnels," *Journal of Highway and Transportation Research and Development (English Edition)*, vol. 12, no. 2, pp. 59–66, 2018.
[29] P. Asteriou and G. Tsiambaos, "Effect of impact velocity, block mass and hardness on the coefficients of restitution for rockfall analysis," *International Journal of Rock Mechanics and Mining Sciences*, vol. 106, pp. 41–50, 2018.
[30] D. Toe, A. Mentani, L. Govoni, F. Bourrier, G. Gottardi, and S. Lambert, "Introducing meta-models for a more efficient hazard mitigation strategy with rockfall protection barriers," *Rock mechanics and rock engineering*, vol. 51, no. 4, pp. 1097–1109, 2018.
[31] W. Wang, S. Shi, Y. Liu, and G. Wang, "The application of expanded polystyrene cushion layer in oblique flexible net systems for rockfall protection: a new attempt," *International Journal of Protective Structures*, vol. 9, no. 2, pp. 141–156, 2017.
[32] A. Q. Bhatti, "Computational modeling of energy dissipation characteristics of expanded polystyrene (EPS) cushion of Reinforce concrete (RC) bridge girder under rockfall impact," *International Journal of Civil Engineering*, vol. 16, no. 11, pp. 1635–1642, 2018.
[33] Y. Bi, Y. Du, S. He et al., "Numerical analysis of effect of baffle configuration on impact force exerted from rock avalanches," *Landslides*, vol. 15, no. 5, pp. 1029–1043, 2018.
[34] B. Yu, W. Yi, and H. Zhao, "Experimental study on the maximum impact force by rock fall," *Landslides*, vol. 15, no. 2, pp. 233–242, 2017.
[35] S.-l. Zhang, X.-g. Yang, and J.-w. Zhou, "A theoretical model for the estimation of maximum impact force from a rockfall based on contact theory," *Journal of Mountain Science*, vol. 15, no. 2, pp. 430–443, 2018.
[36] P. Yan, J. Zhang, Q. Fang, and Y. Zhang, "Numerical simulation of the effects of falling rock's shape and impact pose on impact force and response of RC slabs," *Construction and Building Materials*, vol. 160, pp. 497–504, 2018.
[37] Q. X. Yang and B. S. Guan, "Test and research on calculating method of falling stone impulsive force," *Journal of the China Railway Society*, vol. 18, no. 1, pp. 101–106, 1996.
[38] H. S. Yu, *Cavity Expansion Methods in Geomechanic*, Science Press, Beijing, China, 2002.
[39] S. M. He and Y. Wu, "Research on cushioning mechanism of new-typed energy dissipative rock shed," *Chinese Journal of Rock Mechanics and Engineering*, vol. 29, no. 5, pp. 926–932, 2010.